Available online at www.eccomasproceedia.org
Eccomas Proceedia COMPDYN (2023) 3520-3531

ECCOMAS
Proceedia

COMPDYN 2023
9th ECCOMAS Thematic Conference on
Computational Methods in Structural Dynamics and Earthquake Engineering
M. Papadrakakis, M. Fragiadakis (eds.)
Athens, Greece, 12-14 June 2023

# EVALUATION OF SIMULATED GROUND MOTIONS FOR SEISMIC ASSESSMENT OF A STEEL FRAME STRUCTURE USING MULTI-CRITERIA SELECTION AND SCALING APPROACH BASED ON EVOLUTIONARY ALGORITHMS

**Manolis Georgioudakis[1], Shaghayegh Karimzadeh[2], Michalis Fragiadakis[1] and Paulo B. Lourenço[2]**

[1]School of Civil Engineering
National Technical University of Athens, Zografou Campus, Greece
e-mail: {geoem, mfrag}@mail.ntua.gr

[2] Civil Engineering Department, ISISE, ARISE
University of Minho, Campus of Azurem, Guimaraes, Portugal
e-mail: {shaghkn, pbl}@civil.uminho.pt

---

**Abstract.** *Recently, simulated ground motion records have supplanted real records as a key alternative. Unlike real motions, simulations encompass various intensities, source-to-site distances, and site characteristics. However, determining whether they are appropriate for engineering applications takes time and effort. Another challenging topic is the proper selection and scaling of ground motion records to assess the seismic performance of structures. This study aims to investigate the difference between the real and simulated motions selected according to the code design spectra. Simulations are accomplished through the stochastic finite-fault method, considering the uncertainty of the rupture of the North Tabriz Fault Plane in northwestern Iran, one of the hazardous regions with a seismic gap. A real ground motion dataset with consistent seismological characteristics is compiled. The records are selected and scaled through a multicriteria approach using the evolutionary algorithm. In this approach, the mean spectrum and the (period-depended) dispersion fit best with the target spectrum and its dispersion. Variations in real and simulated record sets are assessed using several ground motion intensity metrics. This study also investigates the effectiveness of the simulated motions for seismic demand evaluation of a three-story steel moment frame.*

**Keywords:** Simulated ground motions, Selection, Scaling, Evolutionary algorithms, Steel Moment Frame.

---

doi: 10.7712/120123.10657.20906

## 1 Introduction

In recent times, simulated ground motion records have emerged as a significant alternative to real records. These records offer a wide range of intensities, source-to-site distances, and site characteristics that are not easily accessible through real records. However, the suitability of simulated records for engineering applications requires a considerable amount of time and effort for thorough evaluation. Furthermore, selecting and scaling ground motion records in a proper manner for the evaluation of seismic performance of structures poses significant challenges. Recent research endeavours have centred on the examination of simulation effectiveness utilising diverse methodologies across the world, covering a broad spectrum of engineering implementations. These include seismic assessment evaluations of distinct structures or investigations into seismic loss and risk assessments [1, 2, 3, 4, 5].

This study aims to investigate the difference between the real and simulated motions selected according to the code design spectra. Simulations are accomplished through the stochastic finite-fault method, considering the uncertainty of the rupture of the North Tabriz Fault Plane (NTFP) in northwestern Iran, one of the hazardous regions with a seismic gap. A real ground motion dataset with consistent seismological characteristics is compiled. The records are selected and scaled through a multi-criteria approach using the evolutionary algorithm. In this approach, the mean spectrum and the (period-depended) dispersion fit best with the target spectrum and its dispersion. Variations in real and simulated record sets are assessed using several ground motion intensity metrics. This work also investigates the effectiveness of the simulated motions for seismic demand evaluation of a three-story steel moment frame.

## 2 Simulated Ground Motion Records

Simulated records are generated through the stochastic finite-fault method, considering the uncertainty of the rupture of the NTFP in Northwestern Iran, one of the hazardous regions with a seismic gap (Fig. 1). NTFP is an active fault with a length of greater than 120 km, having a dextral strike-slip mechanism and an approximate right-lateral slip rate of 8 mm per year [6]. In spite of high seismicity of the region (it has the potential of rupturing with an approximated magnitude of 7.7), there is lack of recorded ground motions for moderate-large magnitude events in the instrumental area.

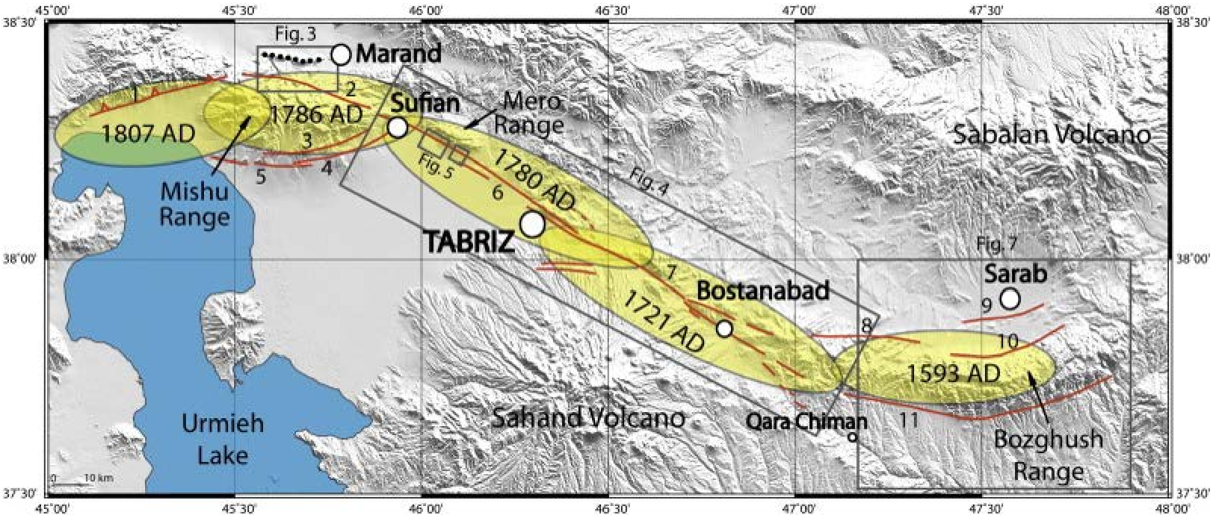

Figure 1: The North Tabriz Fault Plane located in Northwestern Iran [6].

In this study, potential scenario earthquakes with different moment magnitudes ($M_w$) are simulated to evaluate the seismic damage of a benchmark structure. For ground motion simulation of the scenario earthquakes, the stochastic finite-fault method is used. The simulation methodology is introduced by Motazedian et al. [12] and employs a finite-fault model comprised of point-source models as introduced by Boore. The method simulates the frequencies of engineering interest practically compared to the other approaches. Simulations of the scenario events are performed within the EXSIM platform. The simulation technique subdivides the rectangular fault plane into sub-faults with smaller dimensions, each of them having a $\omega^{-2}$ shape. The rupture initiates from the hypocenter, which is located in the center of one of the sub-faults. Then, rupture propagation achieves from the hypocenter to the other sub-faults in a radial direction with a constant rupture velocity. The technique uses a dynamic corner frequency approach in order to conserve the total radiated energy at high frequencies irrespective of the sub-fault size. The amplitude of the shear wave acceleration spectrum for the $ij$-th sub-fault in the frequency domain is obtained as follow:

$$A_{ij}(f) = CM_{0ij}H_{ij}\left[(2\pi f)^2 / \left[1+\left(\frac{f}{f_{cij}}\right)^2\right]\right] e^{\frac{-\pi f R_{ij}}{Q(f)\beta}} G(R_{ij})A(f)e^{-\pi\kappa f} \tag{1}$$

where:

$$\begin{aligned} C &= \tfrac{R^{\theta\phi}\sqrt{2}}{4\pi\rho\beta^3} \\ M_{0ij} &= \tfrac{M_0 S_{ij}}{\sum_{k=1}^{nl}\sum_{l=1}^{nw} S_{kl}} \end{aligned} \tag{2}$$

in which $C$ is the scaling factor, $R^{\theta\phi}$, $\rho$, $\beta$, $M_{0ij}$ and $S_{ij}$ correspond to radiation pattern, density, shear-wave velocity, seismic moment and relative slip weight of the $ij$-th sub-fault, respectively. The term $H_{ij}$ is a scaling factor given as follows:

$$H_{ij} = \sqrt{\left[N\cdot\sum\left(\frac{f^2}{1+(f/f_0)^2}\right)\Big/\sum\left(\frac{f^2}{1+(f/f_{0ij})^2}\right)\right]} \tag{3}$$

where N corresponds to total number of sub-faults and $f_{0ij}$ expresses the dynamic corner frequency of the $ij$-th sub-fault. This scaling factor is employed for conserving the spectral shape at high-frequency portion. The dynamic corner frequency is given as:

$$f_{cij}(t) = (N_R(t))^{-\frac{1}{3}} \cdot 4.9 \cdot 10^6 \beta \left(\frac{\Delta\sigma}{M_{0_{ave}}}\right)^{\frac{1}{3}} \tag{4}$$

which is a function of stress drop ($\Delta\sigma$), number of ruptured sub-faults ($N_R(t)$) at the time $t$, and average seismic moment of sub-faults ($M_{0_{ave}} = M_0/N$). The term $R_{ij}$ corresponds to the distance of the $ij$-th sub-fault from the observation point. The quality factor is expressed by the term $Q(f)$. The term $G(R_{ij})$ is the geometric spreading factor as a function of $R_{ij}$. The site amplification factor is shown by $A(f)$. Finally, the term $e^{-\pi\kappa f}$ stands for the high-cut filter, which controls the spectral shape at high frequencies. In this formula, the kappa factor of soils is expressed by $\kappa$.

Finally, the acceleration time history at each site is calculated by summing the contribution of all sub-faults in time domain where the time delay of each sub-fault is taken into account as follows:

$$a(t) = \sum_{i=1}^{nl} \sum_{j=1}^{nw} a_{ij}(t + \Delta t_{ij}) \tag{5}$$

where, $a(t)$ corresponds to the acceleration time series at time $t$, $a_{ij}(t)$ stands for the acceleration time series of the $ij$-th sub-fault and $\Delta t_{ij}$ expresses the appropriate delay time which is defined as the difference of the time when the seismic wave radiates from the $ij$-th sub-fault to the time of reaching the observation point.

## 3 Selection and Scaling of Ground Motion Records

The current state-of-practice is followed by various design codes and guidelines, where the records are *selected* using engineering judgement and some simple filters based on qualitative criteria. Such criteria require that the records have to match the magnitude, fault mechanism, soil conditions of the site of interest [9]. The selected ground motions are subsequently *scaled*, usually so that their their mean spectrum, matches on average and over a wide range of periods the target spectrum. Amplitude scaling to a target acceleration value $S_T(T_i, \zeta)$ is obtained multiplying the ground motion with a scalar $s = S_T(T_i, \zeta)/S_a(T_i, \zeta)$, where $S_a(T_i, \zeta)$ is the spectral acceleration of the unscaled ground motion at $T_i$. The whole process is well-known as *spectrum matching*.

In this study, spectrum matching is performed considering a two-objective mixed-integer optimization problem which is formulated in order to consistently consider both the mean $F_\mu$ and the variability $F_\beta$ [11] functions where:

$$\begin{aligned} F_\mu(\mathbf{X}) &= \sqrt{\textstyle\int_{T_l}^{T_u} \left[\mu_{log}\left(\mathbf{s}^T \mathbf{S}_a(T, \zeta)\right) - log\left(S_T(T, \zeta)\right)\right]^2 dT} \\ F_\beta(\mathbf{X}) &= \sqrt{\textstyle\int_{T_l}^{T_u} \left[\sigma_{log}\left(\mathbf{s}^T \mathbf{S_a}(T, \zeta)\right) - \beta_T(T, \zeta)\right]^2 dT} \end{aligned} \tag{6}$$

In addition, $\zeta$ is the damping ratio of the structure and $\mathbf{s} = [s_1, s_2, \dots s_N]^T$ and $\mathbf{S}_a(T, \zeta)$ are the vectors contain the scaling factors and the spectral accelerations of each record, while $T_l$ and $T_u$ define the period range of interest. If $T_1$ is the fundamental vibration period, EC8 recommends that $T_l = 0.2T_1$ and $T_u = 2.0T_1$ and $\beta(T, \zeta)$ is the logarithmic dispersion (function of the period T), assumed, or provided by a ground motion model (GMM). Subsequently, the problem formulation is written as follows:

$$\begin{aligned} &\text{minimize} \quad [F_\mu(\mathbf{X}), F_\beta(\mathbf{X})] \\ &\text{subject to:} \quad g_k(\mathbf{X}) \leq 0 \end{aligned} \tag{7}$$

where $g_k(\mathbf{X})$ are the constraints of the problem. Eq. (7) describes a Pareto problem, whose solution is a set of optimum solutions. This is further explained in Fig. 2 where a set of optimum solutions is plotted in a graph; the two axes represent the two objective functions: $F_\mu$ and $F_\beta$. This curve is known as the “Pareto front” (red solid line). Pareto problems have meaning only if the objectives functions are “competing”. In the problem at hand, due to the nature of the two objectives functions, i.e. mean and its variability, $F_\mu$ and $F_\beta$ are always competing and thus the shape of the Pareto front will always be convex. This allows to select the three optimum design solutions shown in Fig. 2 as ‘A’, ‘B’ and ‘C’. Designs ‘A’ and ‘C’ are the optimum designs corresponding to the best optimum design with respect to $F_\mu$ and $F_\beta$, respectively. Design ‘B’ can be defined as the member of the Pareto front that has the minimum distance $min(D)$ from the origin and will always provide a good compromise solution, suitable for engineering practice.

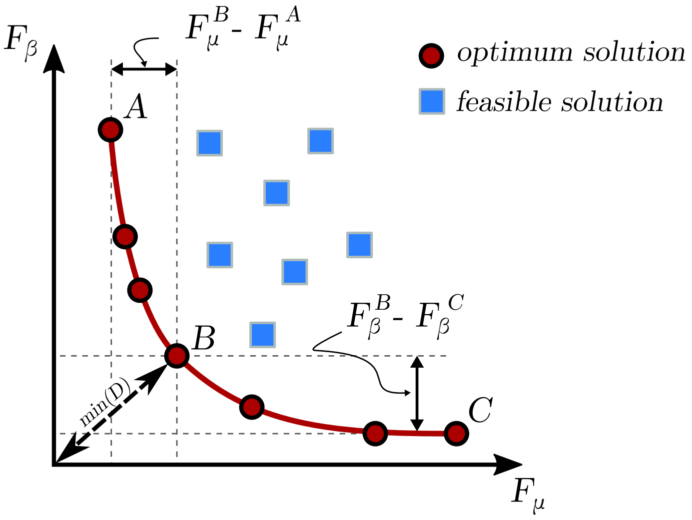

Figure 2: Pareto front solutions and selection of Point B as good compromise solution.

For solving the multi-objective optimization problem we adopt the differential evolution for multi-objective optiomization (DEMO) algorithm [15]. DEMO takes advantage of the differential evolution alorithm [14] in combination with the mechanisms of Pareto-based ranking and crowding distance sorting, used by evolutionary algorithms in multi-objective optimization problems. To preserve a uniformly spread Pareto-front of non-dominated solutions, it uses the following principle: the offspring replaces the parent if it dominates it. If the parent dominates the offspring, the offspring is discarded. Otherwise, when the offspring and parent are non-dominated with regard to each other, the offspring is added to the population. This step is repeated until the number of offsprings created reach the population size. If the population has enlarged, a truncation scheme is applied for the next step of the algorithm. The truncation scheme is based on the non-dominated sorting process which individuals of the same front are evaluated with the crowding distance metric [16]. The truncation ensures that only the best individuals, considering all objective functions, will be in the population.

## 4 Spectrum Matching of Simulated and Real Ground Motion Records

Two sets of ground motions datasets, i.e. *simulated* and *real*, are compiled. Simulations are accomplished through the stochastic finite-fault method, considering the uncertainty of the rupture of the NTFP in north-western Iran. Subsequently, a real ground motion dataset is compiled with consistent seismological characteristics.

### 4.1 Generation of the Ground Motions Datasets

**The Simulated Ground Motion Dataset**: The stochastic finite-fault methodology based on a corner frequency approach as described in Sec. 2 was utilized to conduct ground motion simulations for scenario earthquakes of magnitude ($M_w$) equal to 6.8, 7.1, 7.4 and 7.7 at random nodes in the city centre. The ruptured fault length and width are estimated according to Wells and Coppersmith [17] for scenario events of the same magnitude levels. To account for the aleatory uncertainty of earthquakes, in the entire length of the NTFP, alternative ruptured fault planes and hypocenters are considered. Each magnitude is investigated separately, and multiple ruptured fault lines are generated for each magnitude value. The input model parameters for simulation, which include source, path, and site effects, are adopted from Hoveidae et al. [18] and calibrated accordingly. Finally, the simulated dataset includes 6207 ground motion records in total and were validated using different ground motion models (GMMs), including BA08 [19], AC10 [20], ASB14 [21] and KAAH15 [22]. Fig. 3 illustrates a validation example in terms of peak ground acceleration (PGA) for a scenario event with $M_w$ = 7.1.

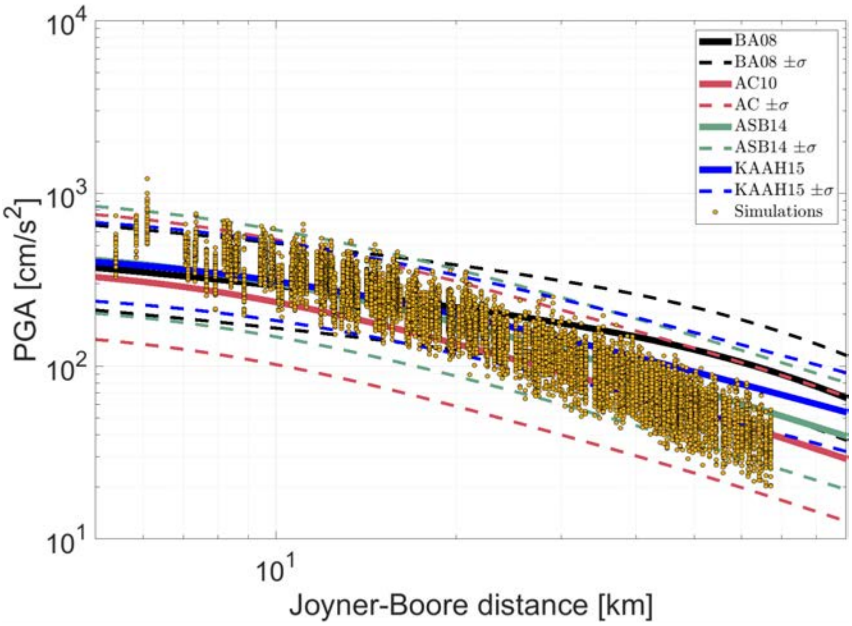

Figure 3: Comparison of PGA against GMMs for $M_w$ = 7.1.

**The Real Ground Motion Dataset**: For the compilation of the real ground motion dataset, the PEER NGA-West2 [24] ground motion records database was used. The database includes 21,336 (mostly) three-component records from 599 events. The parameter space covered by the database is $M_w$ 3.0 to 7.9, closest distance of 0.05 to 1,533 km, and site time-averaged shear-wave velocity in the top 30 m of $V_{S30}$ = 94 m/s to 2,100 m/s. Using consistent seismological characteristics related to NTFP region, the Criteria Set #1 from Table 1 were applied for each parameter to extract a compatible subset of ground motion records. This first search returned a subset of only 30 ground records from 6 events. Hence, to enlarge the real ground motion dataset, an extended range of parameters set were applied (Criteria Set #2) which finally returned 52 ground motion records from 8 events.

| | Parameter | | | | | |
|---|---|---|---|---|---|---|
| Criteria Set | Magnitude | $V_{S30}$ [m/s] | $R_{JB}$ [km] | Depth [km] | Fault Mechanism | Pulse-like |
| #1 | 6.8 - 7.7 | 175 - 375 | 0.5 - 80 | 6 - 18 | Strike-Slip (SS) | No |
| #2 | 6.8 - 7.7 | 30 - 500 | 0.5 - 150 | 6 - 18 | Strike-Slip (SS) | No |

Table 1: Criteria range applied to PEER database.

Fig. 4 shows a comprehensive histogram that portrays various seismological parameters, namely $M_w$, and Joyner-Boore distance ($R_{JB}$), along with ground motion intensity measures, namely PGA and Sa($T_1$) for both the simulated and real datasets compiled. In Fig. 5 the spectra of the two datasets along with their mean spectrum are also depicted.

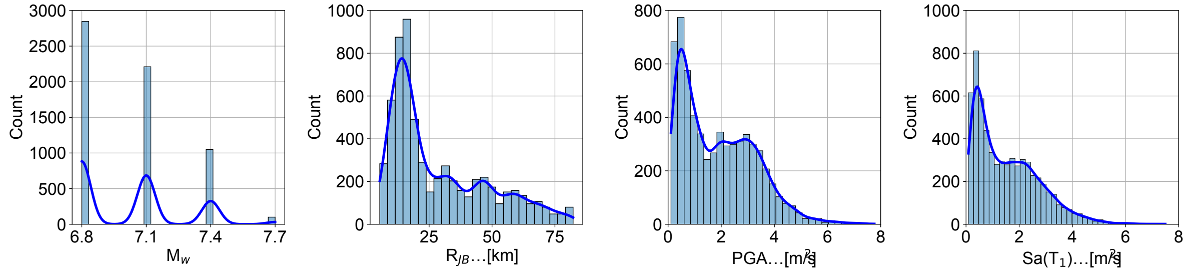

(a) Simulated records

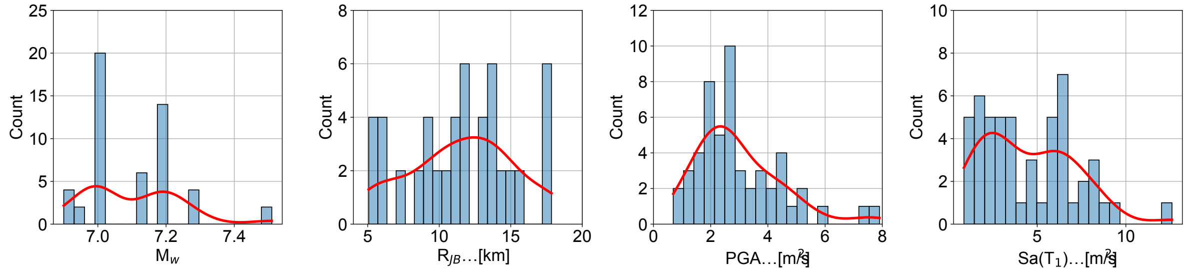

(b) Real records

Figure 4: Histograms of various parameters of the (a) simulated and (b) real ground motion datasets.

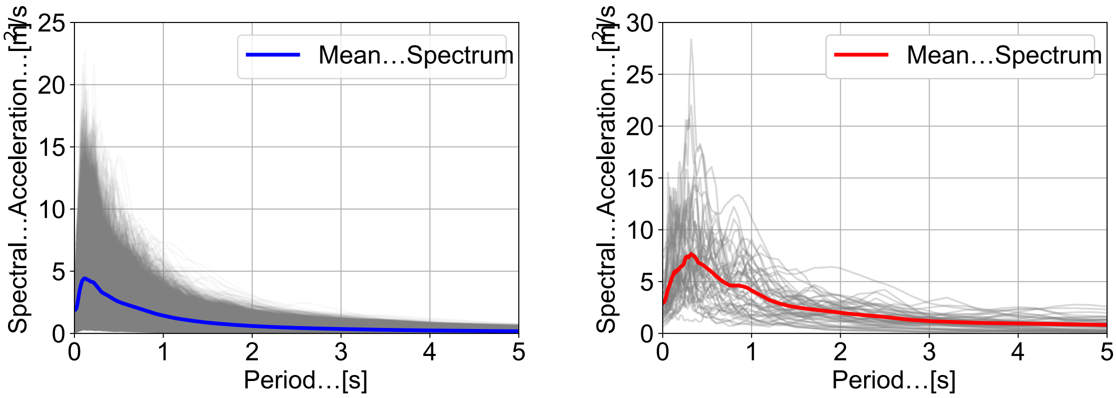

(a) Simulated records (b) Real records

Figure 5: Spectra of the (a) simulated and (b) real ground motion dataset, along with their mean spectrum.

## 4.2 Spectrum Matching Results

Seven ground motion records were selected from the two ground motion datasets (i.e. simulated and real ones) and two-objective optimisation problems was subsequently solved where the mean and the dispersion of ground motion subset are matched to the elastic spectrum of EC8 [7]. The DEMO algorithm was adopted assuming values equal to 200, 0.6 and 0.9 for the population size, the mutation factor and the crossover probability, respectively. For both cases the parameters assumed for the target spectrum, are: peak ground acceleration $\alpha_g = 0.4g$, soil type “A”, damping $\zeta = 2\%$ and importance factor $\gamma_I = 1$. Following EC8 guidelines, we have chosen a period matching range of $0.2 \sim 1.9$ s, assuming that the building’s fundamental period is $T_1$ = 0.93 s. The scaling factors are allowed to vary in the range: $0.1 \sim 2$.

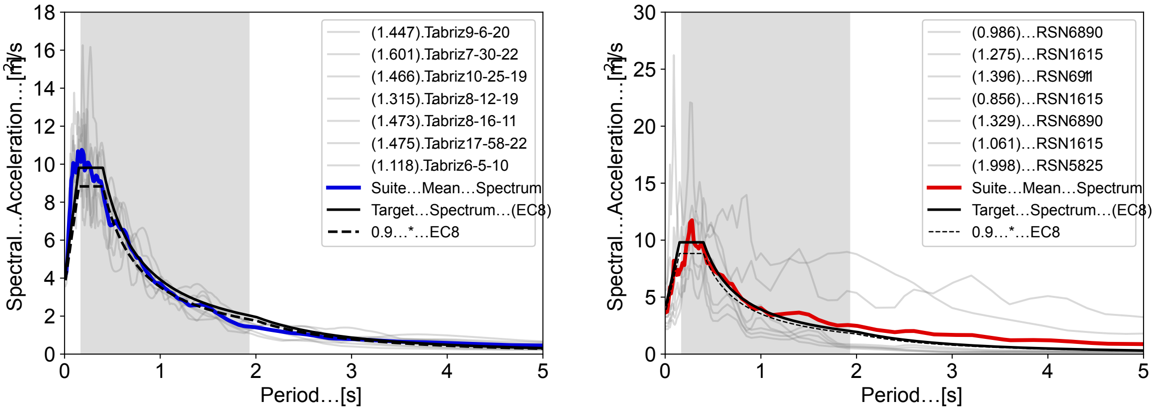

(a) Simulated records

(b) Real records

Figure 6: Spectrum matching results for (a) simulated and (b) real ground motion records. In parenthesis the scale factor of each selected record.

Fig. 6 shows the Pareto front obtained after 300 DE generations for the trade-off solution of both datasets. A comparative analysis of the plots of the two datasets reveals that simulations are capable of generating consistent and evenly-distributed seismological parameters and ground motion intensity levels, in contrast to the real dataset. This underscores the effectiveness of simulated records in providing homogeneous scatteredness of seismological parameters and ground motion intensity levels.

## 5 Impact Investigation on Dynamic Response of a Steel Building

The effectiveness of the simulated motions for seismic demand evaluation of a benchmark structure is also investigated. The benchmark structure is a three-storey steel moment-resisting frame designed for a Los Angeles site and known as the “LA3 building” following the 1997 NEHRP (National Earthquake Hazard Reduction Program) provisions in the framework of the SAC/FEMA program [8]. The dynamic response of the building is dominated by the fundamental mode and has a fundamental period equal to $T_1 = 0.93$ s. All response history analyses were performed in OpenSees [23] using a force-based, beam-column fiber element with five integration sections and a material bilinear with pure kinematic hardening. Rayleigh damping is used to obtain a damping ratio of 2% for the first and the fourth mode.

Fig. 7 shows the distribution of interstorey drift demand when both $F_\mu$ and $F_\beta$ are considered (trade-off solution). The distribution clearly shows a rather small error on the mean value and excellent estimates of the dispersion of the demand when simulated ground motions are considered, compared to the real ones. The reason for this observation is the use of region-specific simulated records compared to real motions that originate from various regions worldwide, resulting in differing spectral shapes and higher dispersion compared to the target spectra. This finding further is supported also from the comparison of various intensity metrics (see Tables 2 and 3), emphasizing the usefulness of simulations in regions with a scarcity of real motions.

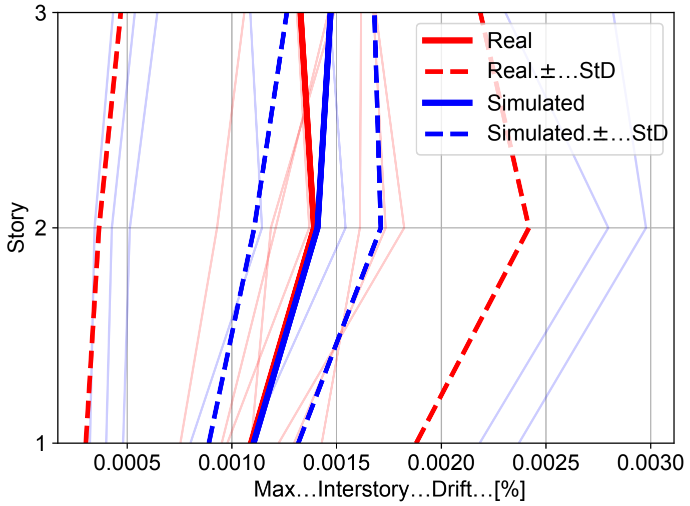

Figure 7: Interstory drifts comparison for LA3 building.

| 🟥 | Record | Scaling Factor | | PGA | PGV/PGA | Sa(T1) | Arias Intensity |
|---|---|---|---|---|---|---|---|
| | | | | $[\mathrm{m/s^2}]$ | [s] | $[\mathrm{m/s^2}]$ | [m/s] |
| 1 | Tabriz9-6-20 | 1.447 | Unscaled | 2.867 | 0.082 | 0.874 | 2.753 |
| | | | Scaled | 4.150 | 0.082 | 1.830 | 3.985 |
| 2 | Tabriz7-30-22 | 1.601 | Unscaled | 2.789 | 0.086 | 1.037 | 2.382 |
| | | | Scaled | 4.465 | 0.086 | 2.659 | 3.814 |
| 3 | Tabriz10-25-19 | 1.466 | Unscaled | 2.422 | 0.093 | 0.606 | 3.439 |
| | | | Scaled | 3.550 | 0.093 | 1.303 | 5.040 |
| 4 | Tabriz8-12-19 | 1.315 | Unscaled | 3.336 | 0.076 | 1.631 | 2.683 |
| | | | Scaled | 4.388 | 0.076 | 2.820 | 3.529 |
| 5 | Tabriz8-16-11 | 1.473 | Unscaled | 2.771 | 0.103 | 0.923 | 2.022 |
| | | | Scaled | 4.081 | 0.103 | 2.002 | 2.979 |
| 6 | Tabriz17-58-22 | 1.475 | Unscaled | 2.770 | 0.111 | 1.985 | 2.845 |
| | | | Scaled | 4.087 | 0.111 | 4.320 | 4.197 |
| 7 | Tabriz6-5-10 | 1.118 | Unscaled | 3.619 | 0.087 | 0.802 | 3.128 |
| | | | Scaled | 4.047 | 0.087 | 1.003 | 3.499 |
| | | Mean Values | Unscaled | 2.939 | 0.091 | 1.123 | 2.750 |
| | | | Scaled | 4.110 | 0.091 | 2.277 | 3.863 |

Table 2: Intensity metrics for simulated dataset.

| 🟦 | Record | Scaling Factor | | PGA | PGV/PGA | Sa(T1) | Arias Intensity |
|---|---|---|---|---|---|---|---|
| | | | | [m/s$^2$] | [s] | [m/s$^2$] | [m/s] |
| 1 | RSN6890_DARFIELD_CMHSS80E | 0.986 | Unscaled | 2.462 | 0.086 | 1.031 | 2.793 |
| | | | Scaled | 2.427 | 0.086 | 1.002 | 2.753 |
| 2 | RSN1615_DUZCE_1062-N | 1.275 | Unscaled | 1.166 | 0.088 | 0.202 | 0.867 |
| | | | Scaled | 1.486 | 0.088 | 0.328 | 1.106 |
| 3 | RSN6911_DARFIELD_HORCN18E | 1.396 | Unscaled | 4.414 | 0.240 | 3.195 | 6.125 |
| | | | Scaled | 6.160 | 0.240 | 6.222 | 8.548 |
| 4 | RSN1615_DUZCE_1062-N | 0.856 | Unscaled | 1.166 | 0.088 | 0.202 | 0.867 |
| | | | Scaled | 0.997 | 0.088 | 0.148 | 0.742 |
| 5 | RSN6890_DARFIELD_CMHSS80E | 1.329 | Unscaled | 2.462 | 0.086 | 1.031 | 2.793 |
| | | | Scaled | 3.273 | 0.086 | 1.823 | 3.713 |
| 6 | RSN1615_DUZCE_1062-N | 1.061 | Unscaled | 1.166 | 0.088 | 0.202 | 0.867 |
| | | | Scaled | 1.237 | 0.088 | 0.228 | 0.920 |
| 7 | RSN5825_SIERRA.MEX_GEO000 | 1.998 | Unscaled | 2.806 | 0.150 | 3.156 | 3.732 |
| | | | Scaled | 5.606 | 0.150 | 12.597 | 7.456 |
| | | Mean Values | Unscaled | 2.234 | 0.118 | 1.288 | 2.578 |
| | | | Scaled | 3.026 | 0.118 | 3.193 | 3.605 |

Table 3: Intensity metrics for real dataset.

## 6 Conclusions

- This study investigated the difference between the real and simulated motions selected according to the code design spectra.
- Two ground motion datasets (simulated and real) with consistent seismological characteristics are compiled.
- The records are selected and scaled through a multicriteria approach using the evolutionary algorithm. In this approach, the mean spectrum and the (period-depended) dispersion fit best with the target spectrum and its dispersion.
- In the context of real records, because the data is scarce, the same event records are used multiple times. However, this issue does not arise for the simulated ones.
- Variations in simulated and real record sets are assessed using several ground motion intensity metrics.
- Investigation of the effectiveness of the simulated motions for seismic demand evaluation of a three-story steel moment frame, emphasizing the usefulness of simulations in regions with a scarcity of real motions.

## ACKNOWLEDGEMENTS

This work was partly financed by FCT/MCTES through national funds (PIDDAC) under the R&D Unit Institute for Sustainability and Innovation in Structural Engineering (ISISE), under reference UIDB/04029/2020, and under the Associate Laboratory Advanced Production and Intelligent Systems ARISE under reference LA/P/0112/2020. Also, it was partly funded by the STAND4HERITAGE project that has received funding from the European Research Council (ERC) under the European Union's Horizon 2020 Research and Innovation Program (Grant Agreement No. 833123) as an Advanced Grant.

## REFERENCES

[1] S. Koboevic, K. Guilini-Charrette, P.X. Castonguay and R. Tremblay (2011). *Selection and scaling of NBCC 2005 compatible simulated ground motions for nonlinear seismic analysis of low-rise steel building structures*. Canadian Journal of Civil Engineering, **38**12.

[2] J. Fayaz, M. Dabaghi and F. Zareian. *Utilization of Site-Based Simulated Ground Motions for Hazard-Targeted Seismic Demand Estimation: Application for Ordinary Bridges in Southern California*. Journal of Bridge Engineering, **25**11, BE.1943-5592.0001634.

[3] S. Karimzadeh, K.Kadas, A. Askan and A. Yakut. *Comparison of real and simulated records using ground motion intensity measures*. Soil Dynamics and Earthquake Engineering, **147**, 106796.

[4] M. Causse, A. Laurendeau, M. Perrault, J. Douglas, L.F. Bonilla and P. Guéguen (2014). *Eurocode 8-compatible synthetic time-series as input to dynamic analysis*, Bulletin of Earthquake Engineering, **12**, pages 755—768.

[5] G. Pousse, L.F. Bonilla, F. Cotton and L. Margerin (2006). *Nonstationary stochastic simulation of strong ground motion time histories including natural variability: Application to the K-net Japanese database*. Bulletin of the Seismological Society of America, **96**(6): 2103.

[6] S. Azad, H. Philip, S. Dominguez, K. Hessami, M. Shahpasandzadeh, M. Foroutan, H. Tabassi and M. Lamothe (2015). *Paleoseismological and morphological evidence of slip rate variations along the North Tabriz fault (NW Iran)*. Tectonophysics, **640–641**, 20-–38.

[7] EN 1998-1 (2004). *Eurocode 8: Design of structures for earthquake resistance – Part 1: General rules, seismic actions and rules for buildings*. European Committee for Standardization.

[8] FEMA-355C (2000). *State of the Art Report on Systems Performance of Steel Moment Frames Subject to Earthquake Ground Shaking*. SAC Joint Venture, EMW-95-C-4770.

[9] J.J. Bommer, A.B. Acevedo (2004). *The use of real earthquake accelerograms as input to dynamic analysis*, Journal of Earthquake Engineering, 8, 43–91.

[10] D. M. Boore (1983). *Strong-motion seismology*. Reviews of Geophysics, **21**(6), 1308–1318.

[11] M. Georgioudakis and M. Fragiadakis (2020). *Selection and scaling of ground motions using multicriteria optimization*, Journal of Structural Engineering (ASCE), **146**(11), 04020241.

[12] D. Motazedian and GM. Atkinson (2005). *Stochastic finite-fault modeling based on a dynamic corner frequency*. Bulletin of the Seismological Society of America, **95**(3), 995-–1010.

[13] NIST Report GCR 11-917-15 (2011). Selecting and Scaling Earthquake Ground Motions for Performing Response-History Analyses, NEHRP Consultants Joint Venture.

[14] K. Price, R. Storn, M. Rainer and J.A. Lampinen (2005). *Differential Evolution: A Practical Approach to Global Optimization*, Springer.

[15] T. Robič and B. Filipič (2005). DEMO: Differential Evolution for Multiobjective Optimization, in *Evolutionary Multi-Criterion Optimization: Third International Conference, EMO 2005*, eds.C.A. Coello Coello, A. H. Aguirre, E. Zitzler, 520–533.

[16] K. Deb, A. Pratap, S. Agarwal, T. Meyarivan (2002). *A fast and elitist multiobjective genetic algorithm: NSGA-II*, IEEE Transactions on Evolutionary Computation, 6(2), 182–197.

[17] D. Wells and K. Coppersmith (1994). *New Empirical Relationships among Magnitude, Rupture Length, Rupture Width, Rupture Area, and Surface Displacement*. Bulletin of the Seismological Society of America, **84**, 974-1002.

[18] N. Hoveidae, A. Fathi and S. Karimzadeh (2021). *Seismic damage assessment of a historic masonry building under simulated scenario earthquakes: A case study for Arge-Tabriz*. Soil Dynamics and Earthquake Engineering, **147**:106732.

[19] D. M. Boore and G. M. Atkinson (2008). *Ground-Motion Prediction Equations for the Average Horizontal Component of PGA, PGV, and 5%-Damped PSA at Spectral Periods between 0.01 s and 10.0 s*. Earthquake Spectra, **24**(1), 99–138.

[20] S. Akkar and Z. Cagnan (2010). *A Local Ground-Motion Predictive Model for Turkey, and Its Comparison with Other Regional and Global Ground-Motion Models*. Bulletin of the Seismological Society of America, **100**(6), 2978—2995.

[21] S. Akkar, M. A. Sandıkkaya and J. J. Bommer (2013). *Empirical ground-motion models for point- and extended-source crustal earthquake scenarios in Europe and the Middle East*. Bulletin of Earthquake Engineering, **12**(1), 359-–387.

[22] Ö. Kale, S. Akkar, A. Ansari and H. Hamzehloo (2015). *A Ground-Motion Predictive Model for Iran and Turkey for Horizontal PGA, PGV, and 5% Damped Response Spectrum: Investigation of Possible Regional Effects*. Bulletin of the Seismological Society of America, **105**(2A), 963—980.

[23] S. Mazzoni, F. McKenna, M.H. Scott and G.L. Fenves (2006). *OpenSEES command language manual*, Pacific Earthquake Engineering Research (PEER) Center.

[24] Ancheta, Timothy D. and Darragh, Robert B. and Stewart, Jonathan P. and Seyhan, Emel and Silva, Walter J. and Chiou, Brian S.-J. and Wooddell, Katie E. and Graves, Robert W. and Kottke, Albert R. and Boore, David M. and Kishida, Tadahiro and Donahue, Jennifer L. *NGA-West2 Database*. Earthquake Spectra, **30**(3), 989–1005.